Planetary and Space Science 90 (2014) 1–9

Contents lists available at ScienceDirect

Planetary and Space Science

journal homepage: www.elsevier.com/locate/pss

Processing OMEGA/Mars Express hyperspectral imagery from radiance-at-sensor to surface reflectance

W.H. Bakker [a,*], F.J.A. van Ruitenbeek [a], H.M.A. van der Werff [a], T.E. Zegers [b], J.H.P. Oosthoek [d,e], S.H. Marsh [c,1], F.D. van der Meer [a]

[a] *University of Twente, Faculty of Geo-Information Science and Earth Observation (ITC), Hengelosestraat 99, 7514 AE Enschede, The Netherlands*
[b] *Utrecht University, Faculty of Earth Sciences, Budapestlaan 17, 3584 CD Utrecht, The Netherlands*
[c] *British Geological Survey, Kingsley Dunham Centre, Keyworth, Nottingham NG12 5GG, England, United Kingdom*
[d] *TNO/Deltares - Geological Survey of the Netherlands, Princetonlaan 6, 3584 CB Utrecht, The Netherlands*
[e] *Jacobs University Bremen, Campus Ring 1, 28759 Bremen, Germany*

A R T I C L E   I N F O

Article history:
Received 24 December 2011
Received in revised form
20 October 2013
Accepted 18 November 2013
Available online 27 November 2013

Keywords:
Mars
Mars Express
OMEGA
Image processing
Transmittance model
Atmospheric correction
3D-filtering
Spatio-spectral filtering
Mineralogy

A B S T R A C T

OMEGA/Mars Express hyperspectral imagery is an excellent source of data for exploring the surface composition of the planet Mars. Compared to terrestrial hyperspectral imagery, the data are challenging to work with; scene-specific transmission models are lacking, spectral features are shallow making them difficult to detect, and field data for validation is mostly not available. Software is available for calibrating the raw data to radiance-at sensor, but a processing methodology for processing the radiance data to surface reflectance is not straightforward. In this paper, we present a processing methodology for converting OMEGA data from radiance-at-sensor to surface reflectance. To overcome specific issues with OMEGA data, we developed novel methods for determining a per-scene transmittance spectrum, performing an atmospheric correction, and filtering systematic and random noise. The processing methodology produces surface reflectance images, from which single-pixel spectra can be extracted to identify surface features. Consistent with several previous studies, our results indicate the presence on the Martian surface of iron-rich clays.

1. Introduction

Mars Express, the European Space Agency's (ESA) first planetary mission to Mars, was launched on June 2, 2003 and inserted in Mars orbit on December 26, 2003 (Bonello et al., 2005). Mars Express carries eight instruments for different science objectives, of which the OMEGA (Observatoire pour la Minéralogie, l'Eau, les Glaces et l'Activité) spectrometer (Bibring et al., 2004) is the most suitable instrument for studying the surface mineralogy of Mars. The instrument consists of three subsystems that cover the spectral ranges of 0.36–1.1 μm (VNIR), 0.93–2.7 μm (SWIR1) and 2.5–5.1 μm (SWIR2). Depending on the altitude of the satellite, the spatial resolution of OMEGA varies from 300 m to 4 km, which makes it an excellent instrument to study the mineralogy of large areas (Gendrin et al., 2005). In that respect it is complementary to NASA's CRISM (Compact Reconnaissance Imaging Spectrometer for Mars) instrument onboard of the Mars Reconnaissance Orbiter (MRO), which has an overall higher spatial resolution of 18 m at best (Bishop and Green, 2006).

The information derived from the OMEGA and CRISM instruments has had a major impact on our understanding of the evolution of Mars. Hydrated minerals and clays were first detected by OMEGA (Bibring et al., 2005, 2006; Poulet et al., 2005), and mafic minerals were distinguished (Mustard et al., 2005). CRISM confirmed the findings of OMEGA, reported a more diverse mineralogy (Mustard et al., 2008; Ehlmann et al., 2009) and detected carbonates (Ehlmann et al., 2008; Michalski and Niles, 2010). Both hydrated minerals and carbonates are important evidence for the presence, now or in the past, of liquid water at the surface or in the subsurface, and hence are important in the context of search for life on Mars (Ehlmann et al., 2011).

Data from OMEGA are available through ESA's Planetary Science Archive (PSA, 2011). The same website offers software for the calibration of the data, named the OMEGA reduction

---

[*] Corresponding author. Tel.: +31 53 4874566.
E-mail addresses: w.h.bakker@utwente.nl (W.H. Bakker), f.j.a.vanruitenbeek@utwente.nl (F.J.A. van Ruitenbeek), harald.vanderwerff@utwente.nl (H.M.A. van der Werff), tanja@geo.uu.nl (T.E. Zegers), j.oosthoek@jacobs-university.de (J.H.P. Oosthoek), stuart.marsh@nottingham.ac.uk (S.H. Marsh), f.d.vandermeer@utwente.nl (F.D. van der Meer).

[1] Now at NGI.

0032-0633/$ - see front matter © 2013 Elsevier Ltd. All rights reserved.
http://dx.doi.org/10.1016/j.pss.2013.11.007

software, Soft07 (ESA - OMEGA team, 2010). This software, which consists of an IDL routine, produces radiance data at the sensor.

Further processing of the radiance data and conversion to surface reflectance have been described in the literature (Langevin et al., 2006; Jouglet et al., 2007; McGuire et al., 2009). A common method used by various researchers is to use a transmission spectrum derived by measuring the transmittance at the base and the summit of Olympus Mons. This method, commonly called volcano scan or empirical transmission function (ETF), was first applied to the OMEGA instrument (Combe et al., 2005; Gendrin et al., 2005) and is also used for the CRISM instrument of the Mars Reconnaissance Orbiter (MRO) (Bishop et al., 2007; Mustard et al., 2008; Wiseman et al., 2010). The ETF is determined once and applied for all successive images by deriving a scale factor. This factor is calculated from the depth of the 2 μm CO_2 feature by applying a band ratio of two bands, one in the absorption feature and one on the shoulder of the feature.

Scene-specific atmospheric transmission models of the Martian atmosphere at the time of the data acquisition are left to the responsibility of each team using the data. This, together with the presence of bad spectral bands in the wavelength regions that cover atmospheric features, makes it difficult to atmospherically correct the radiance spectra using standard techniques employed for terrestrial data (e.g. Gao et al., 2009). Also, calibration targets at the Martian surface that could be used for conversion to surface reflectance are not available, because there are no reflectance spectra that were acquired in situ at the Martian surface with well calibrated instruments.

The spectral features contained by the image data are, compared to remotely sensed hyperspectral data on Earth, shallow, which makes them difficult to differentiate from noise in the data. Difficulties in identifying surface spectral features in OMEGA data mainly arise from the specific configuration of observations (mixing of mineral signatures within a given km-size OMEGA pixel, the presence of dust coating at the surface, remote measurements performed above the dusty atmosphere, spectral resolution, etc.). Analysis of the images shows different types of instrumental artefacts common to this type of imaging spectrometers, likely from a variety of systematic and random sources such as bad detector elements, a nonlinear detector response, spatial striping, spectral spiking, spectral smile, and the image wavelet compression used for transmission (Tragheim et al., 2010; ESA - OMEGA team, 2010; Carter et al., 2012).

In this paper, we present a processing methodology for OMEGA imagery to attempt to overcome the issues associated with the conversion of image spectra from calibrated radiance data at sensor to surface pseudo-reflectance. In two steps the spectra are atmospherically corrected by generating a scene-specific atmospheric transmission model (ATM) and by applying a correction algorithm that is insensitive to bad spectral bands. Systematic and non-systematic noise in the image spectra is reduced by application of normalization methods and spatio-spectral filtering. The resulting pseudo-reflectance data can be further used to extract surface mineralogical information.

2. Processing methodology

Fig. 1 shows the steps involved in the conversion of OMEGA data to pseudo-reflectance.

Raw data were downloaded from the Planetary Science Archive (PSA). The raw data consist of two data sets per scene, one data cube having an extension *QUB*, and a geometry cube with an extension of *NAV*. The calibration of the raw data to radiance is carried out using the public domain software tools Soft07 (ESA - OMEGA team, 2010). The accompanying readme file (SOFT07_readme.txt) provides important information on pre-processing of the OMEGA data set with the Soft07 tools. The result is a number of files used as input in our processing methodology.

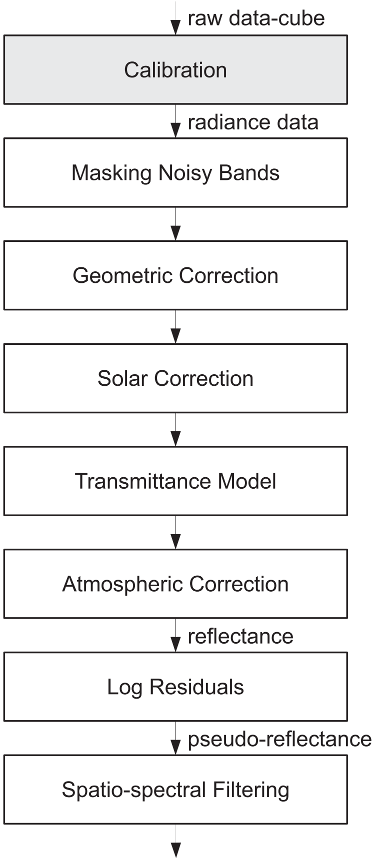

Fig. 1. Processing methodology for OMEGA data. The first step is done using Soft07. The result of this step is radiance data, in which the reliable bands—i.e. those that are not degraded due to cosmic rays or otherwise—are also flagged as useable bands. The remaining steps are done using the HypPy software (Bakker, 2013).

The *geocube* file is used for geocorrection of the image data. It should be noted that the looking directions of the three channels are shifted along track by 1–3 spectels. Furthermore, due to uncertainties in a posteriori orbit reconstruction, the actual location of an observation may be shifted along track or cross track by several pixels. Therefore, a careful adjustment of the geometrical information needs to be performed whenever large local slopes are present.

The *specmars* file contains a Solar spectrum which is used for Solar correction. The *mola* file contains the elevation data of the image derived from the MOLA (Mars Orbiter Laser Altimeter) data (Zuber et al., 1992). The file named *jdat* contains the image data calibrated to radiance values ($W/m^2/sr/\mu m$). The *jdat* file contains all the 352 bands of the OMEGA sensor.

The processing methodology that we developed starts with the identification of noisy spectral bands in the radiance data file *jdat* (Fig. 1). We assume that the dead and hot bands are masked by the Soft07 reading routine. The noisy bands are identified and subsequently masked using a semi-automated process based on their signal-to-noise statistics. Interactively, a threshold for masking bands is determined and the remaining bands are visually inspected. Then the image is geocoded using the location information in the geocube file. Each data set acquired by the three different detectors (VNIR, SWIR1 and SWIR2) is geocoded separately because of misalignments between the three. The OMEGA georeferencing lacks precision and a shift up to a few pixels can occur between the position of a given pixel as indicated in the geocube compared to its real position. The geocoding is visually checked and additional georeferencing steps may be needed for more accurate alignment of the images from the three detectors. In this paper, a spectral subset is made containing the SWIR1 bands and used for further processing. Solar and atmospheric corrections are applied to the geometrically corrected image. The atmospheric correction is performed in two steps: first, an atmospheric transmittance model (ATM) is derived from the image, and second, an atmospheric correction is done using the ATM. This method differs from the standard empirical transmission function (ETF) or “volcano scan” method that uses a model that is derived from an image of Olympus Mons, while we derive a model for each individual image. Subsequently, systematic errors in the image spectra are removed using the log residuals method (Green and Craig, 1985), and random noise is reduced using spatio-spectral filtering.

The procedures for Solar correction, atmospheric correction, logarithmic residuals and 3D spatio-spectral filtering are described in more detail in the following sections. The effects of the processing steps are illustrated using the OMEGA image ORB0422_4. This image covers the Nili Fossae area on Mars, which is mineralogically very diverse (Ehlmann et al., 2011).

The methods described in the processing methodology are implemented in a package called Hyperspectral Python, HypPy (Bakker, 2013). This software was partly developed during the Mars planetary mapping pilot project of the ESA (Tragheim et al., 2010).

2.1. Solar correction

The geocoded image is corrected for Solar irradiance by dividing the radiance data by a Solar irradiance curve at Mars (Fig. 2), available in the *specmars* data file. The specmars curve is obtained from a standard Solar irradiance curve determined at Earth scaled to the Sun–Mars distance. This distance varies between 204.52×10^6 km and 246.28×10^6 km, which means that the Solar irradiance may change by as much as $\pm$ 16%. The Sun–Mars distance of a particular image is available in the header of the cube file. This process only corrects for Solar irradiation and does not take into account topographic effects. Albedo effects caused by the topography of the terrain may still be present.

Prior to Solar correction, the data could be corrected for thermal emission. However, thermal emission only plays a significant role above 3 μm. In this paper we mainly focus on the range between 1 μm and 2.5 μm, where the thermal emission is negligible in the range of the observed daytime Martian surface temperatures of 220–300 K (Jouglet et al., 2007).

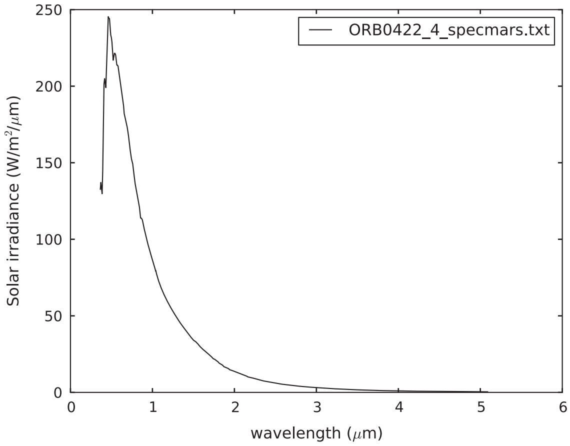

Fig. 2. The *specmars* Solar irradiance curve at Mars for scene ORB0422_4.

2.2. Transmittance model

In order to obtain an atmospheric transmittance model to correct images for the effects of the Martian atmosphere, we use in-scene statistics.

The method estimates atmospheric parameters, the optical path and the wavelength dependency from individual images, by using a standard model for the optical path depending on elevation. For Mars, the elevation is derived from MOLA. This method was first explored by Guan et al. (2006) and Zhu et al. (2010).

Here, we describe our version of this method for obtaining an atmospheric transmittance model (ATM) for all wavelengths by using in-scene statistics. As input, the method takes a Solar-corrected radiance image and an elevation model of the same image. The output is an estimated transmittance curve at the elevation 0 for the current image.

Transmittance t can be expressed as a function of the optical path τ (Wallace and Hobbs, 2006; Petty, 2006):

$$t = e^{-\tau} \tag{1}$$

With the optical path we mean the total radiative transfer path through the atmosphere, which means that it depends on the Solar incidence angle and the sensor viewing angle. For simplicity we assume that these two angles are fairly constant over the entire scene. It should be noted that the optical path τ itself is an exponential function of the height z, which makes the transmittance t a double exponential function of the elevation z (Petty, 2006).

The optical path is proportional to the elevation z:

$$\tau \sim e^{-z/H} \tag{2}$$

The scale height H is a distance over which a quantity, in this case the optical path τ, decreases by a factor of e.

The transmittance t_0 at zero elevation ($z=0$) is then

$$t_0 = e^{-\tau_0} \tag{3}$$

where τ_0 is the optical path at zero elevation.

In the following, it will be shown that Eq. (4) describes the relationship between the transmittance t and the transmittance at elevation zero t_0:

$$t = t_0^{\alpha} \tag{4}$$

Filling in the equations for t and t_0 we get

$$e^{-\tau} = (e^{-\tau_0})^{\alpha} = e^{-\tau_0 \alpha} \tag{5}$$

Taking the log on both sides gives

$$-\tau = -\tau_0 \alpha \tag{6}$$

This gives

$$\alpha = \frac{\tau}{\tau_0} \tag{7}$$

We call α the relative optical path at elevation z.

The observed intensity I can then be expressed by the intensity without atmosphere I^* times the transmittance t:

$$I = I^* t \tag{8}$$

If we substitute t using Eq. (4) this gives the following relation:

$$I = I^* t_0^{\alpha} \tag{9}$$

This equation states that if the transmittance at zero elevation is known and the intensity without atmosphere would be known, then the intensity I is only a function of the relative optical path α.

Unfortunately, both I^* and t_0 are unknown. However, in the following we will show that with a number of assumptions regarding I^*, in fact t_0 can be estimated from an image and its elevation model.

The first observation we make is that, for the spectral range between 1 μm and 2.5 μm, the spectrum is rather flat and that the bands are highly correlated (Fig. 3). This leads to the first assumption that for I^* we might as well take any band within the range of 1–2.5 μm that falls within an atmospheric window. Inside the atmospheric window, the transmittance is 1, or at least very close to 1.

The atmosphere of Mars is composed of 95% carbon dioxide, 3% nitrogen, a tiny fraction of water vapour (±0.03%), and 2% other trace gases (Carr, 2006). Carbon dioxide and water vapour have strong absorption features between 1 μm and 2.5 μm. Absorption by nitrogen and the trace gases does not play a role in this spectral region. For the I^*, we have selected the OMEGA band of 1.714 μm, because we think this band is the best regarding all the factors involved. The band is well within an atmospheric window of carbon dioxide (1.66–1.76 μm) (Prabhakara and Hogan, 1965), and it is outside (or at least at the shoulder of) the broad water absorption feature (1.72–2.03 μm, Fig. 4). At the same time, the band of 1.714 μm is roughly in the middle of the spectral range of 1–2.5 μm. To make the method more robust, to reduce noise or to be less dependent on one band, one could consider an average of wavelengths in an atmospheric window. Here, we only use the 1.714 μm band.

From the previous, it follows that, as an approximation for I^*, we can use $I_{1.7149}$, which is the Solar-corrected radiance I of the 1.7149 μm band of the OMEGA scene:

$$I^* = I_{1.7149} \tag{10}$$

It turns out that if we plot the log–log of the ratio of a particular band I_λ and $I_{1.7149}$ against the elevation z, then we obtain a straight line. In Fig. 5b, all log–log relative intensity pixel values of a scene are plotted against altitude. This particular figure was generated from an OMEGA scene of Nili Fossae (ORB0422_4, Fig. 5a). The elevation of the terrain in this scene ranges from −2970 m to +1731 m, which is an elevation difference of 4701 m. For the figure, the band with most atmospheric absorption (2.0133 μm) is divided by the band with least atmospheric absorption (1.7149 μm). The scatterplot of all 46,848 pixel values against elevation forms a straight line. The regression using a straight line fit has an r^2 of 0.892. This shows that the transmission of the Martian atmosphere can be modelled using a linear fit on the double-logarithm of the relative intensity against the elevation.

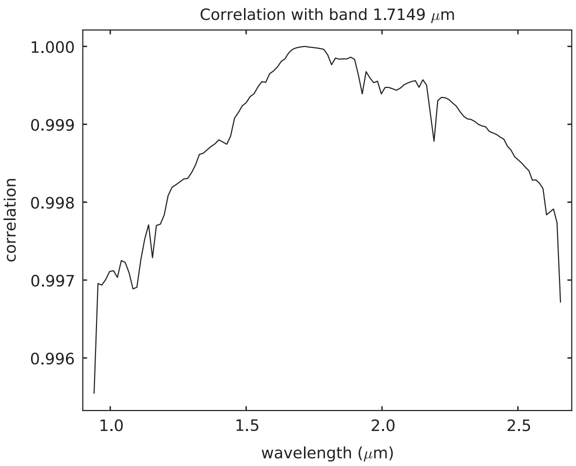

Fig. 3. Correlation of band 1.7149 μm with the other bands. Note that the y-axis runs roughly from 0.996 to 1.000. Graph produced from image ORB0422_4, SWIR1, corrected for geometry, Solar curve and atmosphere.

The only condition that is required for a good estimate of the transmission spectrum is to have enough elevation difference in the scene (our images typically had a height difference of more than 3 km), and the scene should be relatively homogeneous with a relative flat spectrum in the spectral range between 1 μm and 2.5 μm.

The straight-line fit on the log–log can be approximated as

$$-\ln\left(-\ln\left(\frac{I_\lambda}{I_{1.7149}}\right)\right) \approx c_0 z + c_1 \tag{11}$$

The coefficients c_0 and c_1 can be determined using linear regression from the pixel values I_λ against their elevations z.

Transmittance t_0 at zero elevation can be derived from c_1:

$$-\ln\left(\frac{I_\lambda}{I_{1.7149}}\right) = e^{-c_0 z - c_1} = e^{-c_1} e^{-c_0 z} \tag{12}$$

or, by using a double-exponent on both sides,

$$\frac{I_\lambda}{I_{1.7149}} = e^{-e^{-c_1} e^{-c_0 z}} \tag{13}$$

Using Eq. (9) this result can be split into two parts:

$$\alpha = e^{-c_0 z} \tag{14}$$

$$t_0 = e^{-e^{-c_1}} \tag{15}$$

Thus the transmittance at elevation zero t_0 can be derived from the linear regression coefficient c_1.

From Eq. (2) it is clear that the scale height H can be derived from the coefficient c_0:

$$H = \frac{1}{c_0} \tag{16}$$

The scale height only depends on the temperature and the molecular weight of the gas (Eq. (17)), and does not depend on the wavelength:

$$H = \frac{kT}{Mg} \tag{17}$$

with k is the Boltzmann constant 1.38×10^{23} J K^{-1}, T is the mean planetary surface temperature (K), M is the mean molecular mass

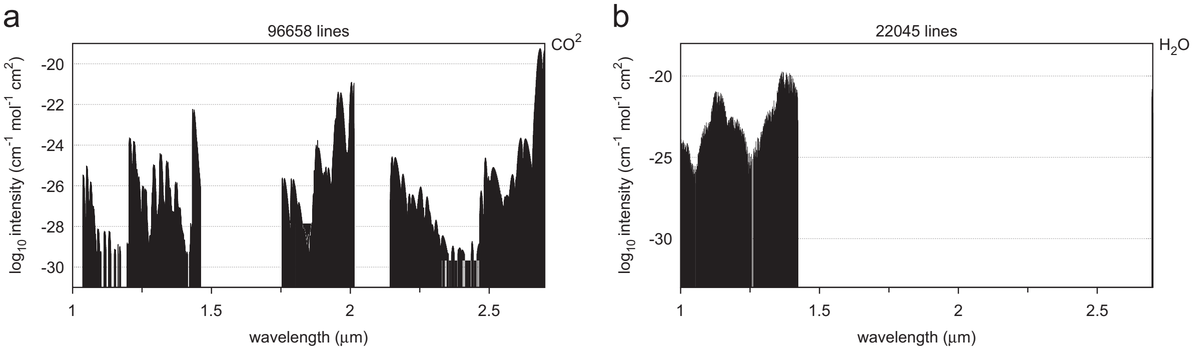

Fig. 4. Log-plot of HITRAN absorption lines of CO_2 and H_2O between 1.0 μm and 2.7 μm. Data generated using the online tool at http://spectralcalc.com. Hitran data for (a) CO_2 and (b) H_2O.

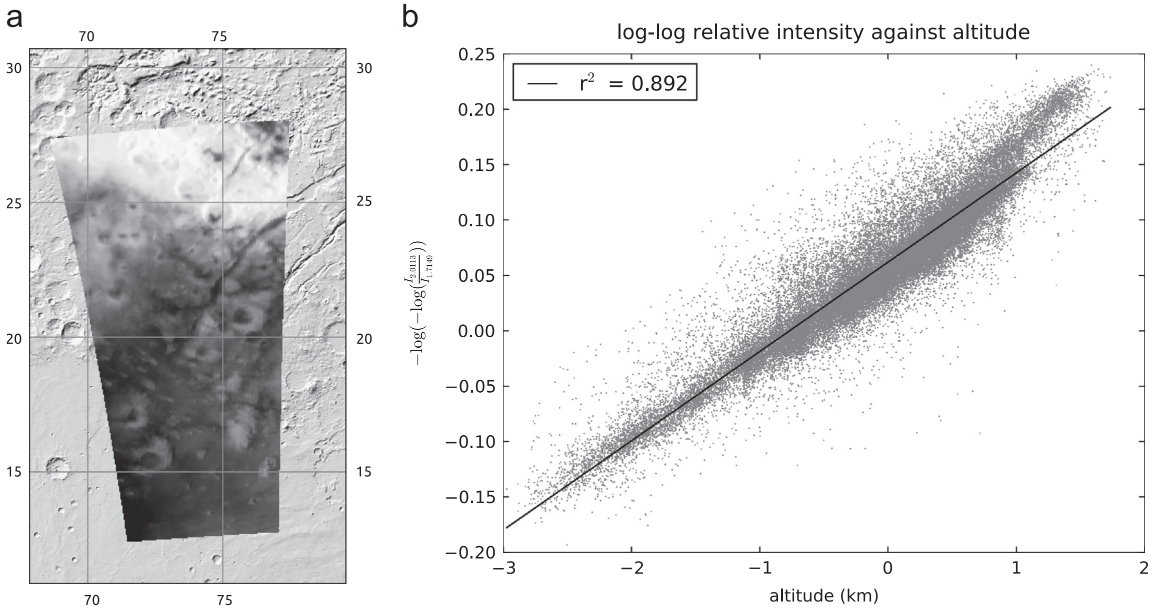

Fig. 5. Log–log of the relative intensity of band 2.0113 μm against altitude. For I^* the band 1.7149 μm of image ORB0422_4 was used (Nili Fossae, left figure). The linear fit on the data has an r^2 of 0.892. (a) Nili Fossae. (b) Log–log relative intensity against altitude.

of dry air (kg), and g is the acceleration due to gravity on planetary surface (m/s^2).

The scale height of the Martian atmosphere is around 11 km (Carr, 2006). This means that the first 33 km contains 95% of the total atmosphere and that even the summit of Olympus Mons is not free of atmosphere, because there is still 15% of the atmosphere left above the top.

The actual scale height determined from the images may differ from 11 km. For instance, for the ORB0422_4 image we find a scale height of 12.41 km. The most plausible cause of a difference in scale height from one cube to the next is a change in atmospheric temperature. The dependency of the scale height on temperature is shown in Eq. (17).

Our method operates in two steps. In step one the c_0 is determined from the deepest absorption feature between 1.8 μm and 2.2 μm. In step two, c_1 for every wavelength is determined by keeping c_0 constant.

Next to CO_2, water vapour is an important absorbent in the range of 1–2.5 μm. It must be noted that, because of the different molecular weight, the theoretical scale height (Eq. (17)) for water vapour is different and that the transmission spectrum generated is only valid for CO_2. In fact, because the H_2O molecule is much lighter than CO_2, the scale height for water vapour is 2.44 times larger than carbon dioxide as the molecular weight of H_2O is 18 g/mol and of CO_2 is 44 g/mol. However, the role of water vapour in an atmosphere is complex. On Earth the scale height deviates considerably from its theoretical scale height (Makarieva and Gorshkov, 2010). Also the role of water vapour in the Martian atmosphere may be more complex than was previously understood (Maltagliati et al., 2011). Because the fraction of water ($\pm 0.03\%$) is tiny compared to CO_2 (95%), we only considered the scale height of CO_2.

To get an indication of the robustness of the method to derive transmittance spectra, the image is divided into 100 random subsets and the minimum and maximum transmittance curves are determined from these 100 subsets. The minimum and maximum values are plotted together with the derived transmittance curve of the entire image. The amount of variation between the minimum and the maximum gives an indication of the confidence interval of the derived transmittance spectrum for a particular image. The confidence level of the transmittance spectrum derived from the scene ORB0422_4 is high (Fig. 6).

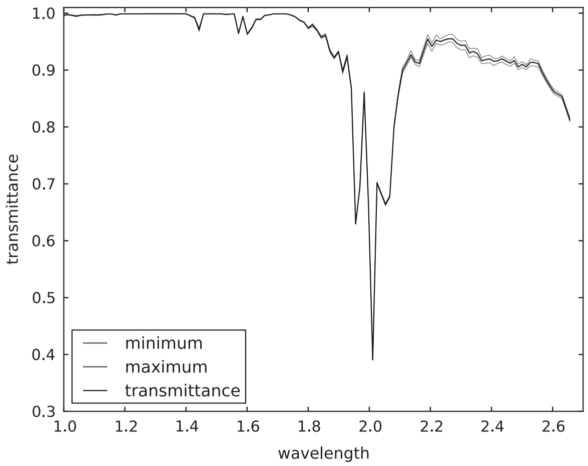

Fig. 6. Derived transmittance spectrum at zero altitude for the OMEGA scene ORB0422_4. The minimum and maximum are an indication for the quality of the obtained transmittance spectrum.

2.3. Atmospheric correction

In our method of atmospheric correction the scaling of the ATM is determined by calculating the local “busyness”' (Dondes and Rosenfeld, 1982) of all the bands in the spectral range between 1.8 μm and 2.2 μm. The local busyness is the sum of the absolute differences of the values of adjacent bands. The local busyness is a function of the atmospheric correction factor, which is the relative optical path α (Eq. (7)). The optimum α is where the local busyness has its minimum. This method is insensitive to bad bands, because a bad band only adds a constant to the local busyness, but does not change the shape of the curve. Furthermore, the local busyness curve as a function of α appears to be a smooth curve with only a single minimum. This means that a simple minimum finding function using the downhill simplex algorithm suffices to find the α, for which the local busyness is minimal.

The optical path τ can be expressed in terms of the incoming and outgoing radiation respectively I^* and I (Milliken et al., 2007):

$$\tau = -\ln\left(\frac{I}{I^*}\right) \tag{18}$$

The transmission t is equal to the ratio of I and I^*:

$$t = \frac{I}{I^*} \tag{19}$$

We define a relative optical path α with respect to a standard (average) Martian atmosphere. The relationship between the standard optical path τ, the relative optical path α and the standard transmittance t_0 then becomes

$$e^{-\alpha\tau} = t_0^{\alpha} \tag{20}$$

The relative optical path α can be estimated from spectra by assuming that the spectrum of a pixel must be smooth in the spectral region between 1.8 μm and 2.2 μm. On the other hand, the CO_2 absorption feature around 2.0 μm is not smooth at all and has a triplet with three distinct absorption peaks (Figs. 4a and 6). This triplet can be used to estimate the effect of the atmosphere. The transmittance t_0 can be scaled by modifying the relative optical path α in such a way that the resulting spectrum is as smooth as possible. We use a local busyness operator for expressing smoothness.

The local busyness is minimized by multiplying the spectrum with a scaled version of the transmission spectrum. In other words, we minimize the relative optical path α such that the following expression is minimal:

$$local\ busyness(\alpha) = \sum_{1.8\ \mu m}^{2.2\ \mu m} \left| \frac{I_j}{{t_0}_j^{\alpha}} - \frac{I_{j+1}}{{t_0}_{j+1}^{\alpha}} \right| \tag{21}$$

where t_0 is the standard transmission spectrum of the Martian atmosphere and I is the observed intensity. The index j denotes the spectral band number of the OMEGA sensor.

It must be noted that light travels through the atmosphere twice and that the α models the entire radiative path through the atmosphere.

Once the factor α is known the atmospheric correction can be done by dividing I by t_0^{α}:

$$I_{corr} = \frac{I}{t_0^{\alpha}} \tag{22}$$

The method works well for wavelengths up to 3.5 μm. After roughly 3 μm the influence of thermal radiation becomes noticeable and the correction model becomes much more complex.

As mentioned before, factor α is the relative optical path of the Martian atmosphere (Eq. (7)). The optical path is, amongst others, related to the elevation of the Martian surface. The factor α is recorded for every pixel, and can be compared to the elevation model of the MOLA to check the consistency. In general, the image containing the factor α is more noisy than MOLA. However, in some locations, like in deep fossae or deep craters, MOLA is over-generalized, whereas the image with the factors α shows more details in these areas.

The elevation z of the terrain can be derived from the scale height H and α (Eqs. (14) and (16)):

$$z = -H \ln(\alpha) \tag{23}$$

The atmospherically corrected image represents surface reflectance (Fig. 1). Systematic and random noise still present in the data can optionally be removed using the two following steps.

2.4. Logarithmic residuals

The reflectance image may still contain systematic errors caused by the instrument or the atmosphere. Ratio techniques with spectra of homogeneous terrain have been used to correct for such errors (Loizeau et al., 2007; Bishop et al., 2007; Jouglet et al., 2007). This step is necessary to bring out the shallow features in the reflectance spectra of surface materials. A disadvantage of this method is that the reference spectrum must typically be hand-picked from a homogeneous area.

For removing systematic errors we optionally apply the logarithmic (log) residuals method. One advantage of this method is that the conversion to pseudo-reflectance does not require *a priori* knowledge of the site. The log residuals method is a two-step normalization in which the spectra of the pixels are normalized first and then divided by the mean spectrum of the whole image (Green and Craig, 1985).

The purpose of the log residuals method is to remove systematic errors present in the scene that are caused by, for instance, albedo effects (caused by topography) and atmospheric effects. Removing atmospheric effects only works if the atmosphere is constant over the entire scene. At the same time, the method also assumes that the composition of the surface that is covered by the image is rather heterogeneous. If the image contains a spectral feature that is present in the entire image then it will have disappeared in the resulting image. Such a feature will only be visible in the SLUB spectrum (Eq. (24)). One disadvantage of log residuals method is that the resulting spectrum is a ratioed spectrum and the result is not absolute reflectance but pseudo-reflectance.

There are different ways to do the double normalization (CSIRO, 2002). The first method calculates the geometric mean rather than the arithmetic mean. The geometric mean can be calculated efficiently in log space, hence the name of the method 'log residuals.' The difference between the arithmetic and geometric means is not dramatic. The quick (kwik) residuals method uses the arithmetic mean rather than the geometric mean. However, for the correction of multiplicative effects, such as remaining atmospheric effects, the log residuals works best.

To make the mean spectrum of the entire image less sensitive to noise, a statistical method is used to determine this spectrum. The statistical least upper bound (SLUB) spectrum is determined as follows (per band):

$$SLUB_i = \min((scene\_avg_i + N * scene\_stdev_i), scene\_max_i) \tag{24}$$

in which $scene\_avg_i$ is the scene's average value for band i, $scene\_stdev_i$ is the scene's standard deviation for band i, and $scene\_max_i$ is the scene's maximum value for band i. To make the algorithm less sensitive to noise, the top 1% of the values are ignored. N is a user-supplied factor, which is typically 3 standard deviations. In a normal distribution only 1% of the values would be larger than the mean plus 3 times the standard deviation.

The SLUB spectrum is a spectrum constructed from relatively bright—but not the brightest—values in the image. If N is set to 0, then the SLUB spectrum is equal to the scene average spectrum.

2.5. Spatio-spectral filtering

For the purpose of removing unsystematic (random) noise we optionally apply a 3-dimensional median or mean filter to the image. The filter does a 3D convolution of a small 3 × 3 × 3 kernel over the entire 3D image data cube (Du et al., 2005). Using a 3D spatio-spectral filter has the advantage that it simultaneously filters the spatial as well as the spectral information. Therefore it can take more values into account (more smoothing), while at the same time the filter remains compact. The latter results in less filter artefacts in the image.

In order to control the degree of smoothing, three different 3D-filters kernels are currently implemented, using a 7-element kernel for least smoothing, using a 19-element kernel for medium smoothing, and using a 27-element kernel for most smoothing (Fig. 7). All elements have equal weight.

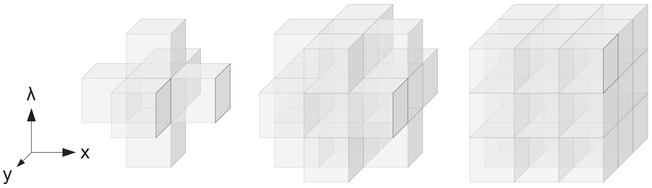

Fig. 7. 3D spatio-spectral filter kernels used. x and y are the spatial dimensions (rows and columns) in the image; λ represents the spectral dimension (wavelength).

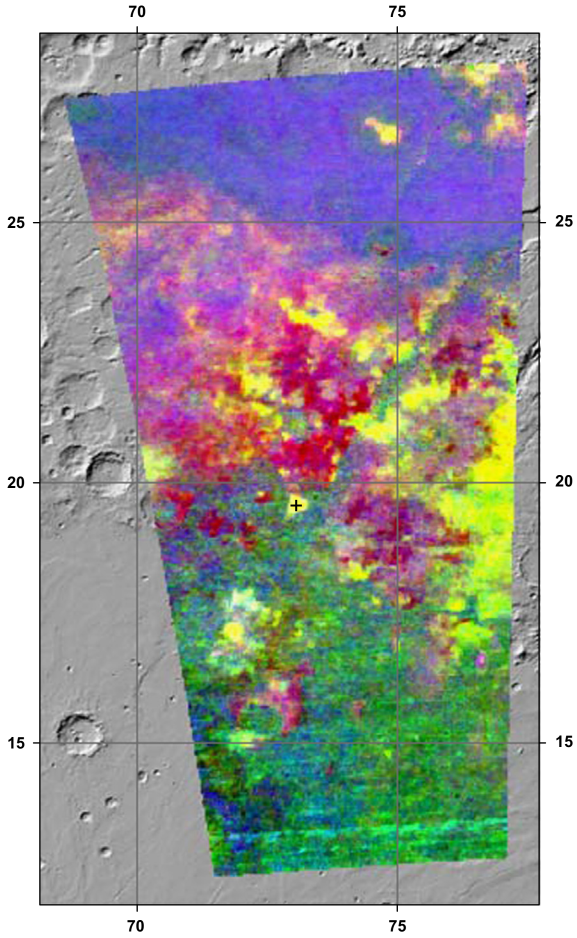

Fig. 8. Colour composite of spectral parameters BD1900, D2300 and D2400 that were calculated from image spectra (Pelkey et al., 2007) for scene ORB0422_4. BD1900 responds to absorption feature at 1.9 μm produced by water. D2300 and D2400 to a drop in the reflectance spectra caused by absorption features near 2.3 μm and 2.4 μm respectively. Point P indicated by the cross is at $19^\circ 33'37''\mathrm{N}, 73^\circ 3'46''\mathrm{E}$. (For interpretation of the references to colour in this figure caption, the reader is referred to the web version of this paper.)

In the example of the Nili Fossae image (Fig. 8) we use the 7-element median filter (Fig. 9c and d). Compared to averaging, median filtering is more edge-preserving and less sensitive to outlier values. However, because median filtering requires sorting of values, it is a rather time-consuming operation.

3. Results and discussion

The effects of the various processing steps on a single-pixel spectrum extracted from OMEGA scene ORB0422_4 (point P, indicated by cross '+' in Fig. 8) are shown in Fig. 9a–c.

Fig. 9a shows calibrated radiance spectra that were produced by the OMEGA reduction software, Soft07. The radiance curve has the general shape of the Solar radiance curve and contains prominent absorption features near 2 μm caused by atmospheric CO_2. Correction for the Solar irradiance curve modifies the general shape of the curve and enhances absorption features of atmospheric gases (Fig. 9b, bottom). Atmospheric correction results in a removal of atmospheric features, for instance the deep absorption features near 2 μm of CO_2 (Fig. 9b, top). The resulting curve shows absolute reflectance. Effects of systematic and random noise are still clearly present, for instance near 1.17 μm (Fig. 9b, N). Further processing of the image by logarithmic residuals removes systematic noise (Fig. 9c, bottom) and spatio-spectral filtering removes noise and enhances the overall spectral shape and spectral features that are most likely produced by surface materials (Fig. 9c, top). In addition, the spatio-spectral filter reduces incoherent noise in the spatial domain (Fig. 9d).

The resulting pseudo-reflectance curve of the pixel shows distinct absorption features at 1.91 μm and near 2.30 μm, and a smaller feature near 1.43 μm (Fig. 9c, A, B and C). The positions and shapes of these features together with the overall curved shape of the spectrum could indicate the presence of iron-rich clays, such as nontronite, at the Martian surface. This interpretation is in line with those of other studies in this area (Poulet et al., 2005, 2008; Ehlmann et al., 2011).

The ATM method we present here is calculated from in-scene statistics and this has several advantages. One advantage is that the ATM takes into account the variability (seasonal, diurnal and other) of the atmosphere regarding CO_2 and H_2O. Although water in the atmosphere is complex and not well-understood. The ATM provides an alternative transmittance model in case the ETF contains biases that are specific to the Olympus Mons scenes from which it was derived. Furthermore, the ATM fits the current state of the sensor regarding bad bands, spectral response function, and calibration status.

Since the ETF is derived from one snapshot of the atmosphere it may not represent the atmospheric condition of a different scene. The ETF is not corrected for the state of the sensor at the moment of acquisition of the current scene. The response function of sensor may have degraded and calibration coefficients may need updating. The ETF may contain artefacts due to the mineralogy present at Olympus Mons, which may differ from the current scene.

The following problems or disadvantages are identified for our ATM and correction method. The statistics of the scene may contain errors due to a remaining misregistration with the MOLA elevation model. However, misregistration is in the order of a few pixels and only gives problems in the steepest areas which occurs at most in a few percent of the pixels. Our ATM only corrects for gaseous absorption (mainly CO_2), while the effect of aerosols may be considerable. The contribution of aerosols to the signal is difficult to model (Vincendon et al., 2007), hence we make no attempt to correct for aerosol effects. The ATM may not work for scenes that have height differences less than 2 km. In this case one could generate an ATM from a scene that is close in location and time of acquisition, or one could fall back to using the ETF derived from Olympus Mons. If we compare our ATM (Fig. 6) with the ETF published by the OMEGA team (Jouglet et al., 2007, Fig. 2), then the ATM has an obvious downward trend between 2.2 μm and 2.5 μm. Correlation is insensitive to bias or offset, which means that even though the bands are highly correlated (Fig. 3) there may still be differences in albedo. In general, reflectance spectra of many minerals seem to have a maximum around 2 μm and drop off toward the shorter and longer wavelengths. Trying to take this into account would seriously complicate the equations under Section 2.2, and worse, be mineral dependent. However, we think that not taking this into account only results in the flattening of the overall shape of the output spectra, while we are mostly

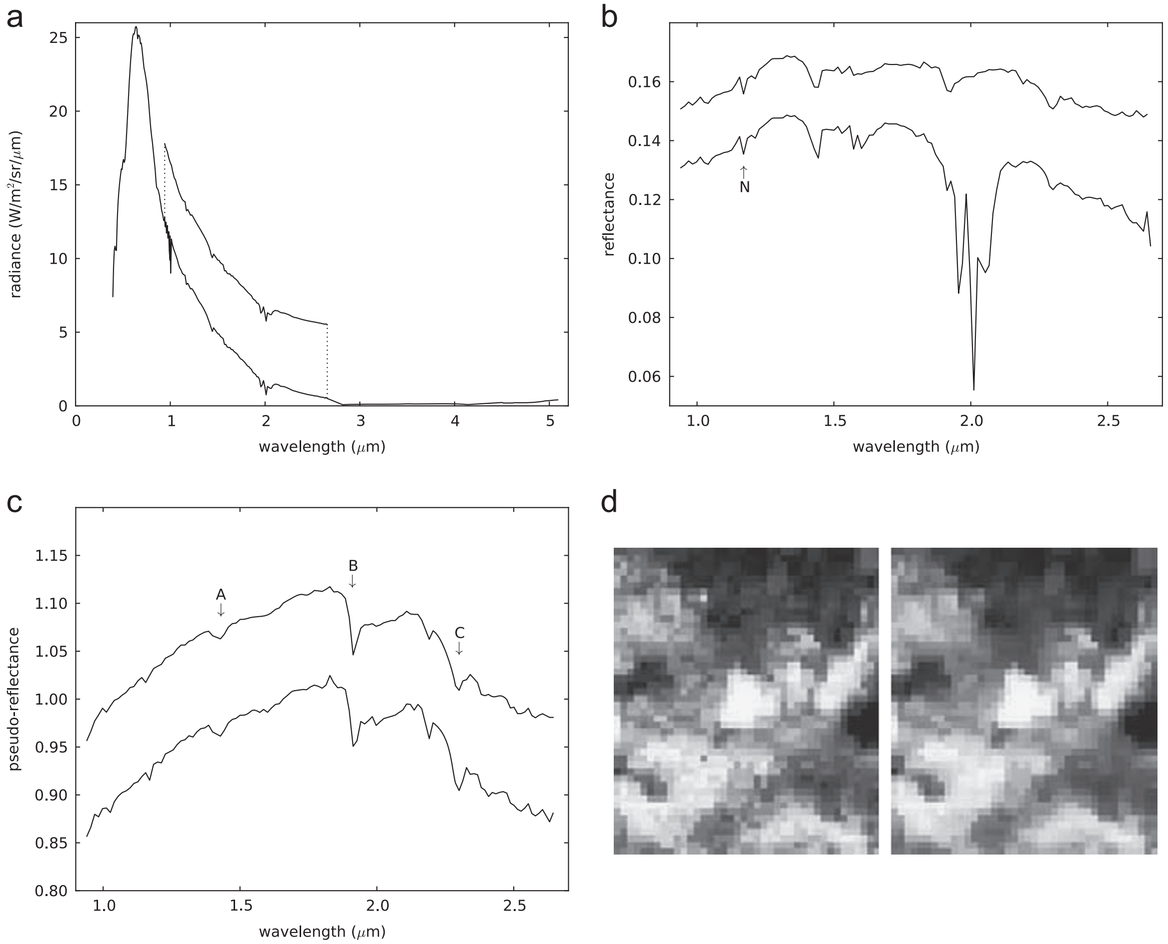

Fig. 9. Spectral and spatial data as processed for point *P* in scene ORB0422_4. (a) Bottom, radiance curve at the sensor; top, spectral subset of the SWIR1 (offset for clarity). (b) Bottom, data corrected for Solar irradiance; top, data corrected for atmosphere (offset for clarity). (c) Bottom, data corrected with log residuals; top, data filtered with 3D median filter with a 7-element kernel (offset for clarity). (d) The effect of the 3D median filter with a 7-element kernel; left, log residual image of band 1.7149 μm; right, 3D filtered data. Point *P* is at the center.

interested in the absorption features, which are well-preserved in the correction process.

The advantages of the local busyness method of atmospheric correction are the following. The local busyness operator is simple and fast. The curve in which the minimum must be found is smooth, has a single minimum, and a simple algorithm suffices to find this minimum. The method is robust with respect to bad bands. Unlike the ratio method that is commonly used for calculating the scaling, the local busyness method does not need to be changed when a different band, or, worse, when yet another band goes bad. The method does not need an elevation model. The advantage of this is that it is not prone to errors or generalizations introduced in MOLA and that it is not sensitive to misregistration between the image and the elevation data. Possible misregistrations make all areas with relatively steep slopes suspect. And last, with a proper model of the built-up of the Martian atmosphere, the elevation could in fact be derived from the relative optical paths α. The local busyness method may not work if the surface materials do not have a flat spectrum around 2 μm. For instance, CO_2 ice has absorption features very similar to CO_2. However, most of the CO_2 ice occurs at south of the 60°S latitude, and we were mainly interested in minerals that have absorption features around 0.9 μm (iron-bearing minerals) or between 2.1 μm and 2.4 μm (phyllosilicates, carbonates, sulphates, etc.).

4. Summary and conclusion

In this paper we describe a complete processing methodology for converting calibrated radiance-at-sensor OMEGA images to surface reflectance images. A method is introduced for deriving atmospheric transmission model (ATM) from the OMEGA image itself. This has the advantage that the ATM reflects the atmospheric condition and the state of the sensor at the exact time of acquisition. We present a new method for atmospheric correction that is insensitive to bad spectral bands. Log residuals is used for correcting systematic errors, and spatio-spectral filtering is applied for reducing random noise. In-scene statistics are used, which avoids subjective bias and enables automatic processing of the OMEGA images. The processing methodology produces surface reflectance images, from which single-pixel spectra can be extracted for the interpretation of surface mineralogy of Mars. Consistent with several previous studies, our results indicate the presence on the Martian surface of iron-rich clays.

The processing chain presented here provides an alternative to existing processing methods. The complete chain or parts of it may be applied to solve specific issues related to the processing of OMEGA images.

Acknowledgements

We thank J.-P. Bibring (Principal Investigator of the OMEGA instrument) and the European Space Agency for the provision of OMEGA data and the Soft07 calibration software. Yves Langevin and an anonymous reviewer are thanked for their constructive comments that helped significantly improve the manuscript.

References

Bakker, W.H., 2013. HypPy Hyperspectral Python Software Package. ⟨http://www.itc.nl/personal/bakker/hyppy.html⟩.

Bibring, J.-P., Langevin, Y., Gendrin, A., Gondet, B., Poulet, F., Berthé, M., Soufflot, A., Arvidson, R., Mangold, N., Mustard, J., Drossart, P., 2005. the OMEGA Team, 2005. Mars surface diversity as revealed by the OMEGA/Mars Express observations. Science 307 (5715), 1576–1581.

Bibring, J.-P., Langevin, Y., Mustard, J.F., Poulet, F., Arvidson, R., Gendrin, A., Gondet, B., Mangold, N., Pinet, P., Forget, F., 2006. the OMEGA Team, 2006. Global mineralogical and aqueous Mars history derived from OMEGA/Mars Express data. Science 312 (5772), 400–404.

Bibring, J.-P., Soufflot, A., Berthé, M., Langevin, Y., Gondet, B., Drossart, P., Bouyé, M., Combes, M., Puget, P., Semery, A., Bellucci, G., Formisano, V., Moroz, V., Kottsov, V., Bonello, G., Erard, S., Forni, O., Gendrin, A., Manaud, N., Poulet, F., Poulleau, G., Encrenaz, T., Fouchet, T., Melchiorri, R., Altieri, F., Ignatiev, N., Titov, D., Zasova, L., Coradini, A., Capacionni, F., Cerroni, P., Fonti, S., Mangold, N., Pinet, P., Schmitt, B., Sotin, C., Hauber, E., Hoffmann, H., Jaumann, R., Keller, U., Arvidson, R., Mustard, J., Forget, F., 2004. OMEGA: Observatoire pour la Minéralogie, l'Eau, les Glaces et l'Activité. In: Wilson, A., Chicarro, A. (Eds.), Mars Express: The Scientific Payload. ESA Special Publication, vol. 1240; 2004, pp. 37–49.

Bishop, J., Green, R., February 2006. Mars polar targets for the CRISM. In: Mars Water Workshop. NASA Ames Research Center.

Bishop, J., Murchie, S., Tornabene, L., Pelkey, S., Gulick, V., Ehlmann, B., Mustard, J., Brown, A., MRO Crism Team, 2007. Characterization of phyllosilicates in Libya Montes and the southern Isidis Planitia region using CRISM and HiRISE images. LPI Contributions 1353, pp. 3294–3297.

Bonello, G., Bibring, J.-P., Soufflot, A., Langevin, Y., Gondet, B., Berthé, M., Carabetian, C., 2005. The ground calibration setup of OMEGA and VIRTIS experiments: description and performances. Planet. Space Sci. 53 (June), 711–728.

Carr, M.H., 2006. The Surface of Mars. Cambridge Planetary Science Series. Cambridge University Press.

Carter, J., Poulet, F., Bibring, J.-P., Mangold, N., Murchie, S.L., 2012. Hydrous minerals on Mars as seen by the CRISM and OMEGA imaging spectrometers: updated global view. J. Geophys. Res. (April), 831–858.

Combe, J.-P., Sotin, C., Mouélic, S.L., Launeau, P., Mustard, J., Gendrin, A., Bibring, J.-P., Gondet, B., Langevin, Y., the OMEGA Science Team, Mar. 2005. Methodology of hyperspectral reflectance data analysis for mineralogical mapping of planetary surfaces: application to OMEGA/Mars-Express images. In: Mackwell, S., Stansbery, E. (Ed.), 36th Annual Lunar and Planetary Science Conference, Lunar and Planetary Institute Technical Report, vol. XXXVI. pp. 1633–1634.

CSIRO, 2002. Log/Kwik/LUB Residuals, The MMTG Manual. CSIRO, p. 46–57.

Dondes, P.A., Rosenfeld, A., 1982. Pixel classification based on gray level and local “busyness”. IEEE Trans. Pattern Anal. Mach. Intell. 4 (January (1)), 79–84.

Du, P., Chen, Y., Yang, Y., Zhang, H., 2005. On the filtering of hyperspectral remote sensing image. In: Li, D., Ma, H. (Eds.), Proceedings of the SPIE, MIPPR 2005: Image Analysis Techniques. Society of Photo-Optical Instrumentation Engineers (SPIE) Conference Series, vol. 6044. pp. 347–353.

Ehlmann, B.L., Mustard, J.F., Murchie, S.L., Bibring, J.-P., Meunier, A., Fraeman, A.A., Langevin, Y., 2011. Subsurface water and clay mineral formation during the early history of Mars. Nature 479 (November (7371)), 53–60.

Ehlmann, B.L., Mustard, J.F., Murchie, S.L., Poulet, F., Bishop, J.L., Brown, A.J., Calvin, W.M., Clark, R.N., Des Marais, D.J., Milliken, R.E., Roach, L.H., Roush, T.L., Swayze, G.A., Wray, J.J., 2008. Orbital identification of carbonate-bearing rocks on Mars. Science 322 (5909), 1828–1832.

Ehlmann, B.L., Mustard, J.F., Swayze, G.A., Clark, R.N., Bishop, J.L., Poulet, F., Des Marais, D.J., Roach, L.H., Milliken, R.E., Wray, J.J., Barnouin-Jha, O., Murchie, S.L., 2009. Identification of hydrated silicate minerals on Mars using MRO-CRISM: geologic context near Nili Fossae and implications for aqueous alteration. J. Geophys. Res. (Planets) 114, 1–33.

ESA - OMEGA team, 2010. OMEGA Reduction Software, SOFT07, March. ⟨ftp://psa.esac.esa.int/pub/mirror/MARS-EXPRESS/OMEGA/MEX-M-OMEGA-2-EDR-FLIGHT-EXT2-V1.0/SOFTWARE/⟩ (last visited October 2011).

Gao, B., Montes, M.J., Davis, C.O., Goetz, A.F.H., 2009. Atmospheric correction algorithms for hyperspectral remote sensing data of land and ocean. Remote Sens. Environ. 113 (Supplement 1), S17–S24.

Gendrin, A., Mangold, N., Bibring, J.-P., Langevin, Y., Gondet, B., Poulet, F., Bonello, G., Quantin, C., Mustard, J., Arvidson, R., Le Mouélic, S., 2005. Sulfates in Martian layered terrains: the OMEGA/Mars Express view. Science 307 (March), 1587–1591.

Green, A.A., Craig, M.D., 1985. Analysis of aircraft spectrometer data with logarithmic residuals. In: Vane, G., Goetz, A. (Eds.), Proceedings of the First Airborne Imaging Spectrometer Data Analysis Workshop. No. 85-41, April 1985. Jet Propulsion Laboratory, JPL, Pasadena, California, pp. 111–119.

Guan, H., Xie, H., Zhu, M., 2006. Development of an alternative Martian atmospheric correction algorithm for OMEGA/Mars Express imagery. In: Mackwell, S., Stansbery, E. (Eds.), 37th Annual Lunar and Planetary Science Conference. Lunar and Planetary Institute Science Conference Abstracts, vol. 37, pp. 1934–1935.

Jouglet, D., Poulet, F., Milliken, R.E., Mustard, J.F., Bibring, J.-P., Langevin, Y., Gondet, B., Gomez, C., 2007. Hydration state of the Martian surface as seen by Mars Express OMEGA: 1. Analysis of the 3 μm hydration feature. J. Geophys. Res. 112, 1–20.

Langevin, Y., Douté, S., Vincendon, M., Poulet, F., Bibring, J.-P., Gondet, B., Schmitt, B., Forget, F., 2006. No signature of clear CO$_2$ ice from the ‘cryptic’ regions in Mars' south seasonal polar cap. Nature 442 (August (7104)), 790–792.

Loizeau, D., Mangold, N., Poulet, F., Bibring, J.-P., Gendrin, A., Ansan, V., Gomez, C., Gondet, B., Langevin, Y., Masson, P., Neukum, G., 2007. Phyllosilicates in the Mawrth Vallis region of Mars. J. Geophys. Res. (Planets) 112 (July), 1–20.

Makarieva, A.M., Gorshkov, V.G., 2010. Potential energy of atmospheric water vapor and the air motions induced by water vapor condensation on different spatial scales. Gen. Phys., 1–37.

Maltagliati, L., Montmessin, F., Fedorova, A., Korablev, O., Forget, F., Bertaux, J.-L., 2011. Evidence of water vapor in excess of saturation in the atmosphere of Mars. Science 333, 1868–1870.

McGuire, P.C., Bishop, J.L., Brown, A.J., Fraeman, A.A., Marzo, G.A., Morgan, M.F., Murchie, S.L., Mustard, J.F., Parente, M., Pelkey, S.M., Roush, T.L., Seelos, F.P., Smith, M.D., Wendt, L., Wolff, M.J., 2009. An improvement to the volcano-scan algorithm for atmospheric correction of CRISM and OMEGA spectral data. Planet. Space Sci. 57 (7), 809–815.

Michalski, J.R., Niles, P.B., 2010. Deep crustal carbonate rocks exposed by meteor impact on Mars. Nat. Geosci. 3 (October), 751–755.

Milliken, R.E., Mustard, J.F., Poulet, F., Jouglet, D., Bibring, J.-P., Gondet, B., Langevin, Y., 2007. Hydration state of the Martian surface as seen by Mars Express OMEGA: 2. H$_2$O content of the surface. J. Geophys. Res. 112, 1–15.

Mustard, J.F., Murchie, S.L., Pelkey, S.M., Ehlmann, B.L., Milliken, R.E., Grant, J.A., Bibring, J.-P., Poulet, F., Bishop, J., Dobrea, E.N., Roach, L., Seelos, F., Arvidson, R.E., Wiseman, S., Green, R., Hash, C., Humm, D., Malaret, E., McGovern, J.A., Seelos, K., Clancy, T., Clark, R., Des Marais, D.J., Izenberg, N., Knudson, A., Langevin, Y., Martin, T., McGuire, P., Morris, R., Robinson, M., Roush, T., Smith, M., Swayze, G., Taylor, H., Titus, T., Wolff, M., 2008. Hydrated silicate minerals on Mars observed by the Mars Reconnaissance Orbiter CRISM instrument. Nature 454 (July), 305–309.

Mustard, J.F., Poulet, F., Gendrin, A., Bibring, J.-P., Langevin, Y., Gondet, B., Mangold, N., Bellucci, G., Altieri, F., 2005. Olivine and pyroxene diversity in the crust of Mars. Science 307 (5715), 1594–1597.

Pelkey, S.M., Mustard, J.F., Murchie, S., Clancy, R.T., Wolff, M., Smith, M., Milliken, R., Bibring, J.-P., Gendrin, A., Poulet, F., Langevin, Y., Gondet, B., 2007. CRISM multispectral summary products: parameterizing mineral diversity on Mars from reflectance. J. Geophys. Res. 112.

Petty, G.W., 2006. A First Course in Atmospheric Radiation, 2nd ed. Sundog Publishing, Madison, Wisconsin.

Poulet, F., Bibring, J.-P., Mustard, J.F., Gendrin, A., Mangold, N., Langevin, Y., Arvidson, R.E., Gondet, B., Gomez, C., 2005. the OMEGA Team, 2005. Phyllosilicates on Mars and implications for early Martian climate. Nature 438, 623–627.

Poulet, F., Mangold, N., Loizeau, D., Bibring, J.-P., Langevin, Y., Michalski, J., Gondet, B., 2008. Abundance of minerals in the phyllosilicate-rich units on Mars. Astron. Astrophys. 487 (2), 41–44.

Prabhakara, C., Hogan, J.S., 1965. Ozone and carbon dioxide heating in the Martian atmosphere. J. Atmos. Sci. 22 (2), 97–109.

PSA, 2011. ESA's Planetary Science Archive. ⟨http://www.rssd.esa.int⟩ (last visited October 2011).

Tragheim, D.G., Marsh, S.H., Pedley, R.C., Napier, B.R., Bateson, L., Smith, A.G., Marchant, A.P., Gunnink, J.L., Oosthoek, J.H.P., Muller, J.-P., Grindrod, P.J., van Ruitenbeek, F.J.A., Bakker, W.H., van der Werff, H.M.A., Martin, P., Zegers, T., 2010. The Mars Planetary Mapping Pilot Project. Final Report, European Space Agency (ESA).

Vincendon, M., Langevin, Y., Poulet, F., Bibring, J.-P., Gondet, B., 2007. Recovery of surface reflectance spectra and evaluation of the optical depth of aerosols in the near-IR using a Monte Carlo approach: application to the OMEGA observations of high-latitude regions of Mars. J. Geophys. Res. (Planets) 112 (July), 8.

Wallace, J.M., Hobbs, P.V., 2006. Atmospheric Science: An Introductory Survey. International Geophysics Series. Elsevier Academic Press.

Wiseman, S.M., Arvidson, R.E., Morgan, F., Wolff, M.J., Morris, R.V., McGuire, P.C., Murchie, S.L., Mustard, J.F., Seelos, F.P., Smith, M.D., 2010. Radiative transfer modeling of the empirical ‘volcano scan’ atmospheric correction: discussion and artifacts. In: Lunar and Planetary Institute, 41st Lunar and Planetary Science Conference.

Zhu, M., Xie, H., Guan, H., 2010. Algorithm development for Martian atmospheric correction and spatiotemporal variation study of atmospheric profiles. Int. J. Mars Sci. Explor. 5, 61–67.

Zuber, M.T., Smith, D.E., Solomon, S.C., Muhleman, D.O., Head, J.W., Garvin, J.B., Abshire, J.B., Bufton, J.L., 1992. The Mars observer laser altimeter investigation. J. Geophys. Res. (Planets) 97 (E5), 7781–7797.